B. TECH. THESIS

Design of Rolling Capsule-type Miniature Robot (RCMR) for Pipe Inspection

Submitted by:

Sakshee Patil | 180003047

Discipline of Mechanical Engineering, Indian Institute of Technology, Indore

Guided by:

Dr. Pavan Kumar Kankar

System Dynamics Lab, Department of Mechanical Engineering, Indian Institute of Technology, Indore, Madhya Pradesh 453552, India

Dr. Ankur Miglani

Microfluidics and Droplet Dynamics Lab, Department of Mechanical Engineering, Indian Institute of Technology, Indore, Madhya Pradesh 453552, India

Dr. Debanik Roy

Scientist, Division of Remote Handling & Robotics, Bhabha Atomic Research Center (BARC) and Professor, Homi Bhabha National Institute (HBNI), Department of Atomic Energy (DAE), Govt. of India, Mumbai 400085, India

Acknowledgements

I'd like to express my heartfelt appreciation to my research supervisors, Dr. Pavan Kumar Kankar and Dr. Ankur Miglani, for their constant encouragement and constructive support, which enabled this work to take its current form. I am thankful to them for giving me the opportunity to carry out such meaningful hands-on research work and providing all the necessary facilities.

I am highly indebted to my mentor, Dr. Debanik Roy, whose encouragement, empathy, and invaluable guidance inspired me to do this work. I am grateful to him for giving me the wonderful opportunity to work on this innovative project that has introduced me to many new things. It was a great privilege and honor to closely work with a professor of his stature.

I'd also like to express my gratitude towards the employees of SVR Infotech, a robotics start-up in Pune with whom the project was affiliated.

Mr. Anoop and Mr. Vipul, M.Tech, IIT Indore, were invaluable in guiding me through the manufacturing and prototyping processes and for that I am grateful. Finally, I'd like to express my gratitude to my family for their love, moral support, and unwavering encouragement. This report would not have been possible without their assistance.

CANDIDATE'S DECLARATION

I hereby declare that the project entitled "Design of rolling capsule type miniature robot (RCMR) for pipe inspection" submitted in partial fulfillment for the award of the degree of Bachelor of Technology in 'Department of Mechanical Engineering' completed under the supervision of Dr. Pavan Kumar Kankar, Dr. Ankur Miglani, IIT Indore and Dr. Debanik Roy, Bhabha Atomic Research Center is an authentic work.

Further, I declare that I have not submitted this work for the award of any other degree elsewhere.

Signature and name of the student(s) with date

(27-05-2022)

CERTIFICATE by BTP Guide(s)

It is certified that the above statement made by the students is correct to the best of my/our knowledge.

Signature of BTP Guide(s) with dates and their designation

Dr. Pavan Kumar Kankar, IIT Indore

24/05/2022 Associate Professor, ME

Dr. Ankur Miglani, IIT Indore

Dr. Ankur Miglani
Assistant Professor
Department of Mechanical Engineering
Indian Institute of Technology Indore
Simrol, Khandwa Road, Indore 453 552, India

25 May 2022

Dr. Debanik Roy, BARC

25/05/2022 Scientist, BARC & Professor, HBNI, DAE

Abstract

Study on the dynamics of activation in real-time and autonomous position control of the target point of a miniature bio-robotic device is a challenging research domain. Miniature robotics involves components that come in compact sizes. Manufacturing these intricate components through the conventional route and getting the right functional output for the desired application is always formidable. The work reports successful CAD design, kinematic simulation and static analysis of a tethered miniature compliant rolling device in Fusion 360, Solidworks and FEAST^{SMT} respectively. This is followed by hardware experimentation, prototyping and fabrication using 3D printing technology. The average device dimension of all the design variations is approximately 20 x 40 mm and thus the component is capable of rolling into a pipeline with a diameter as small as 50 mm. The back lid of the rolling component can act as a mound for a small charged coupled device (CCD) camera which will in turn be used for internal inspection of pipelines and tubes. The work further sheds light on deep learning techniques such as multilabel image segmentation and classification that can be implemented on the images captured by the mounted camera for offline image based defect detection in order to classify and localize internal pipe defects for maintenance.

Table of Content

List of Tables

CHAPTER 1: Introduction

Project statement / Objective(s)

The objective of the study is to customize a rolling capsule-type Miniature Robot (RCMR) for real-life applications of inspection & maintenance. The in-situ rolling motion often gets piggybacked with vibration-generated oscillation and makes the ensemble motion complex in real-time. The RCMR design is inspired by the Biological leech which has characteristic features for its locomotion that can be categorized in two types, namely: a] sticking action and b] sliding motion. One of these motions is perpetual ‘rolling’ with extremely small speed that characterizes the sticking action to a large extent. This report aims to report a representative description on the design characteristics of the “Rolling Capsule” of a prototype bio-robotic leech under consideration and the performance parameters expected from the same. These parameters are based on its application i.e. boiler tube defect detection. The study further aspires to extend the work into image processing of offline images captured by a CCD (charged coupled device) camera incorporated into the rolling capsule design to detect pipeline defects.

Literature Review

Pipelines are one of the primary means of transporting oil and gas from one location to another. Material defects, corrosions and mechanical stress in their manufacturing, storage, or transportation facilities can be disastrous for both mankind and the ecosystem. Thus, timely inspection and maintenance of pipelines becomes crucial for safety. However, most pipelines are located in extreme or hazardous environments where manual inspection solutions become non-economic, time-consuming, possibly dangerous and inaccurate due to human error. [1] Therefore, it is pivotal to develop the state of automated pipeline inspection, assessment and maintenance to ensure the structural integrity of pipeline systems on a regular and vigilant basis. Plenty of research work has been done in developing various aspects of in-pipe inspection robots such as vision and perception, control and motion, actuation etc. [2] Numerous design strategies such as wheeled type robots, leg type robots, screw drive type robots, inchworm type robots etc are available in the market today. However, one aspect that takes a back seat in all these designs is robot size.

Robotic systems are widely used in pipe inspection in a variety of fields, including gas, sewage piping systems and boiler tubes. [3, 4, 5] Tubes typically have thicker walls than regular pipes. Furthermore, most pipe sizes are determined by the inside diameter of the pipe, whereas tube sizes are determined by the outside diameter of the tube which can be as small as 20 mm. Therefore, the principal challenge faced in the design of automated robots for pipes and tubes is the size constraint. There are numerous designs for pipe inspection robots available in the market today, but only a few are capable of operating in pipes with diameters less than 50 mm. Wheeled inspection robots are the most popular amongst the robots designed for pipe inspection where the designs range from wheeled slider-crank mechanisms capable of traversing in a 200 mm pipe [6] to two-chained adaptive wheeled mechanisms with steering capabilities capable of traversing in a 500 mm pipe [7]. However, all designs fall short when it comes to miniaturization since hardly any of the pipe inspection solutions available today are capable of traversing in pipes of diameter less than 80 mm.

Because of the tube size limitation, boiler tube inner surface inspection is a significant challenge. Boilers have hundreds or even thousands of tubes, and steam is generated inside these tubes in most modern boilers. The tubes must be strong enough to withstand the pressure without breaking open and leaking, which is the major cause of boiler shutdown. Comprehensive boiler evaluations are required to accurately identify the mechanisms and root causes of failure, assess operating conditions, and estimate the need for future component replacements. The majority of inspection solutions available today can only inspect the boiler header and cannot travel inside a tube of diameter less than 100mm to inspect the boiler tube condition.

To address this inherent problem, this work proposes a detailed schematic design of a miniature rolling capsule component capable of traversing in a 30 mm horizontal tube with a mini-camera mounted on its back cover. The images captured by this camera would then be used for offline image-based defect detection. The work also extends into deep learning-based methods for detecting surface defects in Steel. The first step in the automated steel surface inspection system is to prepare a robust database of high-resolution images that are representative of different types of surface defects and their severity. The next step involves the extraction of features from these images that helps in categorizing the defects based on their individual characteristics.

Subsequently, the labels are assigned to the different classes of characteristics that are retrieved. Once this dataset is optimized, accurate, and varied to the extent possible, the defect classification and segmentation are explored; wherein a deep learning model is trained over the dataset for defect detection and classification. These steps form the foundation of any automated steel surface inspection system and have been explored over the past decade in varied depth [8-10].

Deep learning methods rely on extensive and robust training data to enable them to generalize well. Since each new image brings a level of newness in terms of the features, the model's performance improves as the dataset of the manually annotated image examples grows. Constructing such a dataset is a time-intensive operation best left to the trained staff. Therefore, The dataset used in this is the open source Severstal Steel Defect Dataset [11]. This dataset consists of 6666 labeled images spread across four types of surface defects in steel plates. The ground truth segmentation masks are also provided in the form of run-length encoded pixels. Literature search reveals that one of the most widely used image segmentation models, namely, the original U-Net architecture, produces a dice coefficient less than 0.5 for this dataset, which is insufficient to justify the use of automation over manual inspection for defect detection. To overcome this discrepancy of needing automation but having poor automation results, thetwo-fold objective of this study is to first maximize the dice score while localizing the defect present in the image, and second, to maximize the multilabel probability estimates.

Work Modules

1. Mechanical Design: A detailed schematic of a Rolling Capsule-type Miniature Robot (RCMR) equipped with a miniature CCD (Charged Coupled Device) camera mount. Development of the 3D CAD Model of the prototype using Fusion 360 software.

2. Kinematic Analysis: Motion Analysis with Solidworks/ADAMS software.

3. Static Analysis: Post-CAD analysis of rheological parameters like stress, deformation / deflection using Finite Element Analysis (FEA) software, FEAST SMT ™.

4. Deep Learning based offline inner pipe inspection: Development of algorithms for evaluation of defect-type, defect-size and defect-spread of images captured by RCMR’S CCD camera using image processing techniques and Deep Learning.

5. Prototyping (3D Printing) and hardware experimentation.

CHAPTER 2: Design Metrics

Design Concept and Variability

The prototype "Rolling Capsule" has a symmetrical layout with different body and ring structures. The most crucial design-parameter is the "Retainer Ring" which gets encompassed between the main body which encloses the motor and the front covering. This particular component is the nucleus of the perpetual rolling motion that gets generated in-situ inside the rolling capsule by virtue of Physics. The ring is press fitted on the motor shaft which needs to generate enough torque to enable the rolling motion. Fig x shows the sequential operation of the retainer ring. The design of the retainer ring can be of various geometrical shapes as listed in table 1. Likewise, the body-structure of the rolling capsule can be either spherical, semi-spherical / barrel shaped or cylindrical.

Table 1. Various Feasible Design Layout of the Rolling Capsule

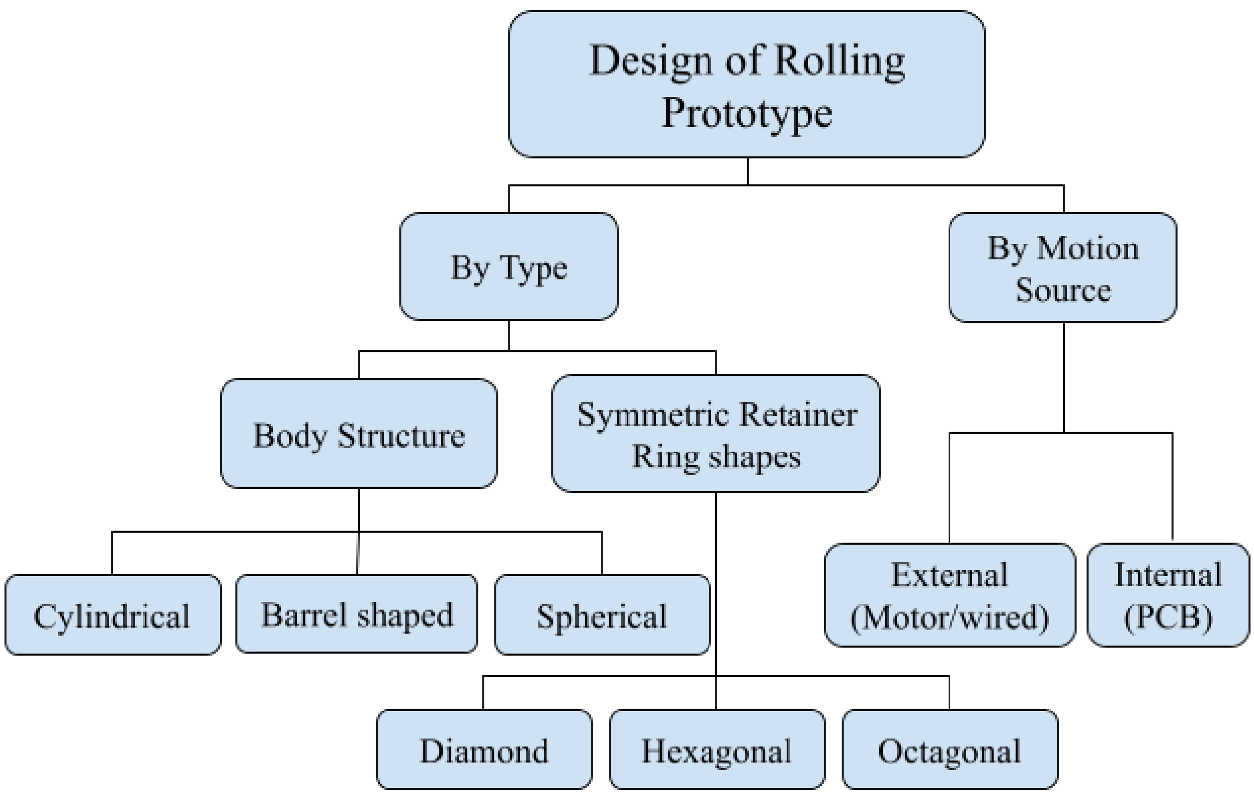

Controller Design

The prototype's primary design requirement is miniaturization, which necessitates the use of a suitable miniature motor with high torque.. The design of the controller for the prototype Rolling Capsule is based on DC motor-based control. The main challenge of the controller is attributed to the real-time control of the perpetual motion vector of the retainer ring (i.e., position & orientation). In other words, control of the rotary motion of the retainer ring through servo-based design is the crux of the control system design of the prototype rolling capsule.

The said control system layout can be invoked through two path-ways, namely: a] with 'tether' and b] wireless (through LAN under wi-fi). Tether-driven control is relatively straight-forward as it is receptive to alterations in the control algorithm & programming and has been implemented. On the other hand, wireless communication & control will involve robust programming in order to combat eventual time-delay & phase-lag issues.

Hardware Requirements:

1. Outer Diameter of capsule <= 20mm. Thus, the outer diameter of the motor is preferably around 15 mm.
2. Stall torque around 100 mNm (approximate value)

Motor Specifications:

1. ART IFACT 4 Pieces of Micro Coreless Motor
    - ➔ 4 Coreless Motor 7x16mm with Shaft Size: 0.8 x 4.7mm
    - ➔ Rated Voltage is 3.7v - 4.2v
    - ➔ Current: 0.1 A-1.5A
    - ➔ Max Speed: 48000 rpm (No Load)
    - ➔ Wire Length 5cm/3"

This high rpm, low torque miniature motor was selected to fulfill the purpose of optimizing the design of the rolling capsule with the smallest parameters

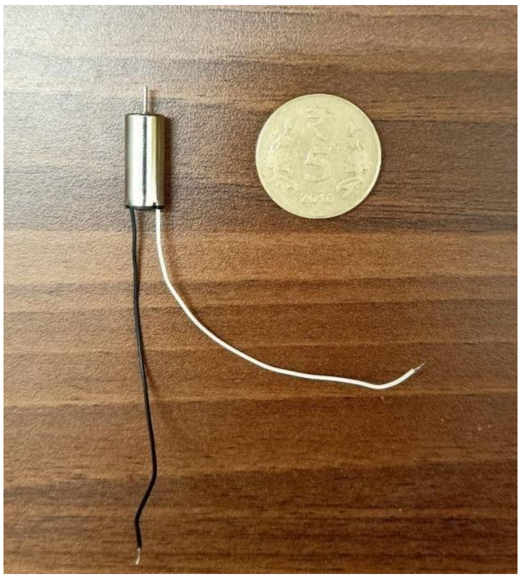

Fig 1. IFACT Motor

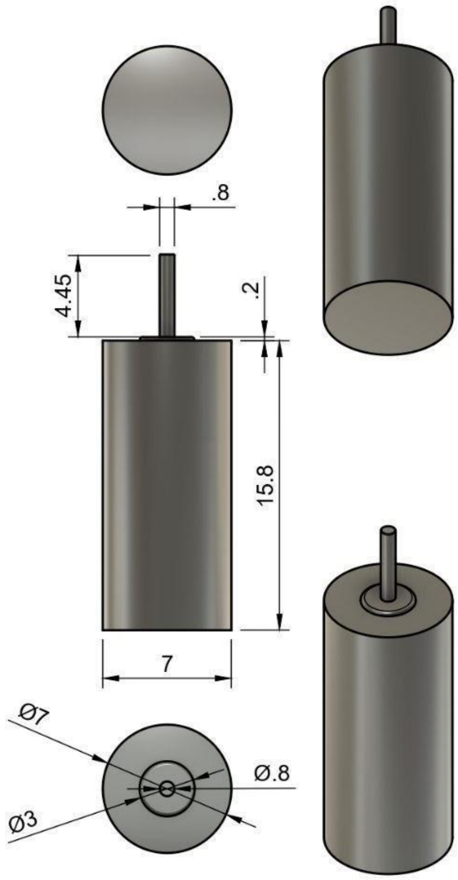

Fig 2. IFACT Motor Schematic

2. N20 Micro Gear 12V 100RPM DC Motor
    - ➔ Rated Operating Voltage: 6 - 12 V
    - ➔ No Load Current: 0.06 A.
    - ➔ Stall Current: 0.75 A
    - ➔ Rated Speed (RPM): 100
    - ➔ Rated Torque(kg-cm): 0.52 – 1.8
    - ➔ Motor Body Size (Diameter): 12 mm
    - ➔ Shaft Diameter: 3 mm
    - ➔ Weight: 10 gm
    - ➔ Output Axial Length: 10 mm
    - ➔ Fuselage w/o Shaft Length: 26 mm

Fig 3. N20 Motor

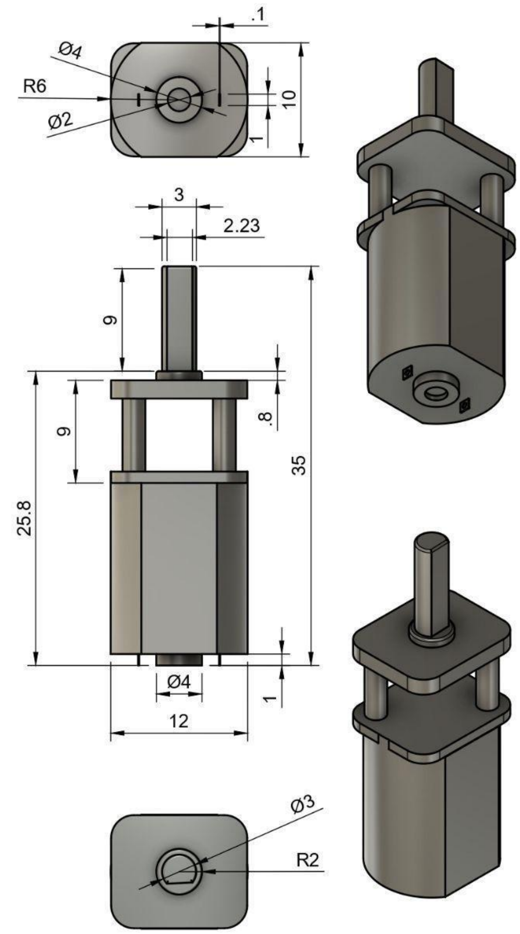

Fig 4. N20 Motor Schematic

3. Precision micro drives: 216-101-16mm-dc-gearmotor-41mm-type
   - ➔ Rated Operating Voltage: 3 V
   - ➔ Rated Speed (RPM): 64
   - ➔ Rated Torque: 115 mNm
   - ➔ Motor Body Size (Diameter): 16 mm
   - ➔ Body length: 40.6 mm
   - ➔ Typical max. output power: 811 mW

Fig 5. Precision Micro Drive Motor

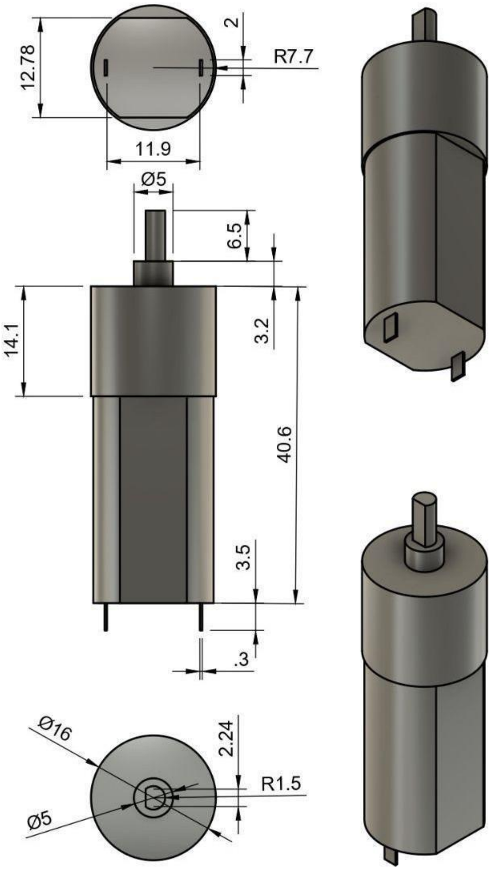

Fig 6. Precision Micro Drive Motor Schematic

Design Schemes: Mechanical Assembly

We can formalize the following layouts for the 'Rolling Capsule' based on the variations detailed in table 1. The schematics below show some of the various combinations that are possible. Figure 7 depicts a cylindrical enclosure designed to house the N20 Micro Gear DC Motor from Figure 4. Similarly, figures 9 and 11 illustrate barrel-shaped and spherical enclosures that were investigated in order to compensate for the slight inclination caused by placing a cylindrical enclosure horizontally on the ground. The various modifications also help in analyzing the effect that the area of the enclosure surface in contact with the ground has on the rolling motion of the prototype. All enclosures contain an inner extrusion of 5 mm from the front end cut out in the shape of the motor to constrain the motor's radial motion as can be seen in the top view of figure 7. The motor shaft protrudes out of the hole provided at the front end. The retainer ring is press fitted on this shaft against the front end of the enclosure to constrain its axial motion. The cylindrical and barrel-shaped prototypes were limited to a diameter of 20 mm, whereas the spherical enclosure has a maximum diameter of 26 mm.

Schematic 1: Cylindrical Body and Diamond ring

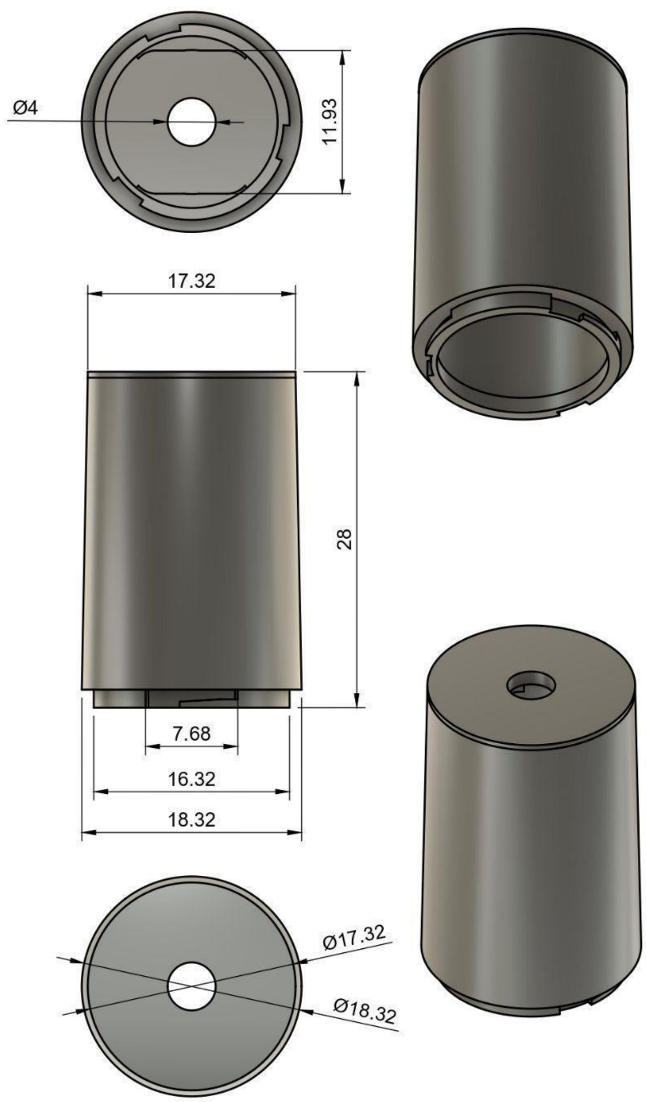

Fig 7. Cylindrical Enclosure

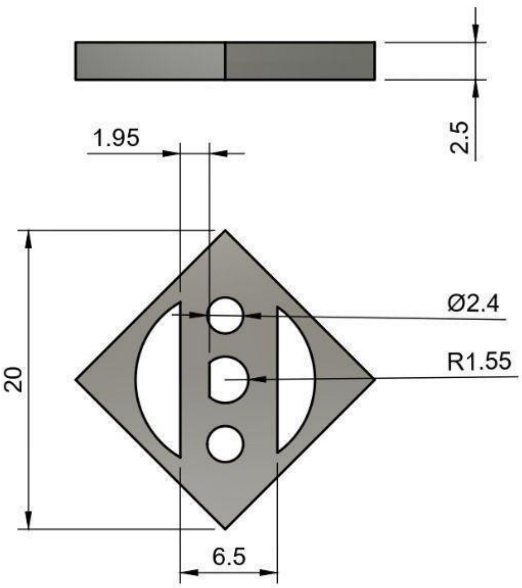

Fig 8. Diamond Retainer Ring

Schematic 2: Semi spherical body and hex ring

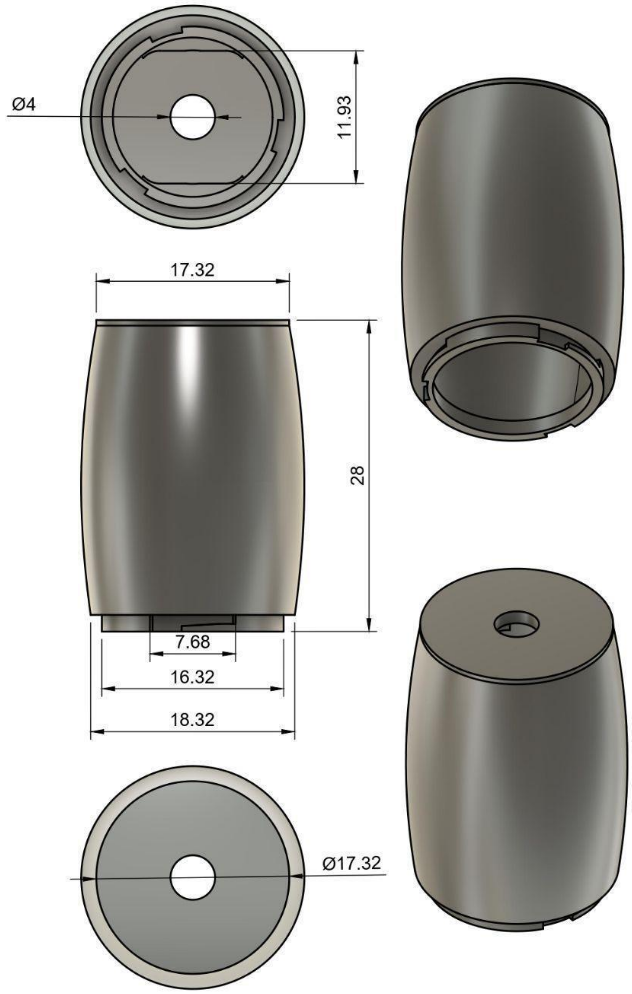

Fig 9. Barrel-Shaped Enclosure

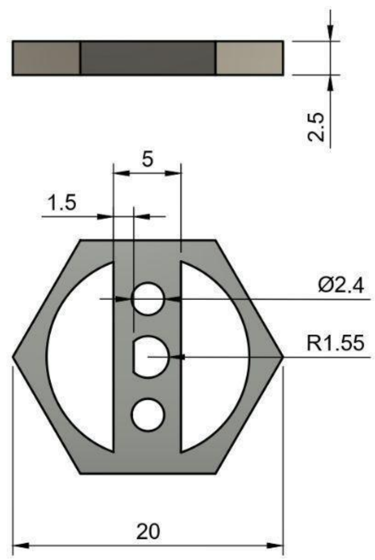

Fig 10. Hexagonal Retainer Ring

Schematic 3: Spherical body and oct ring

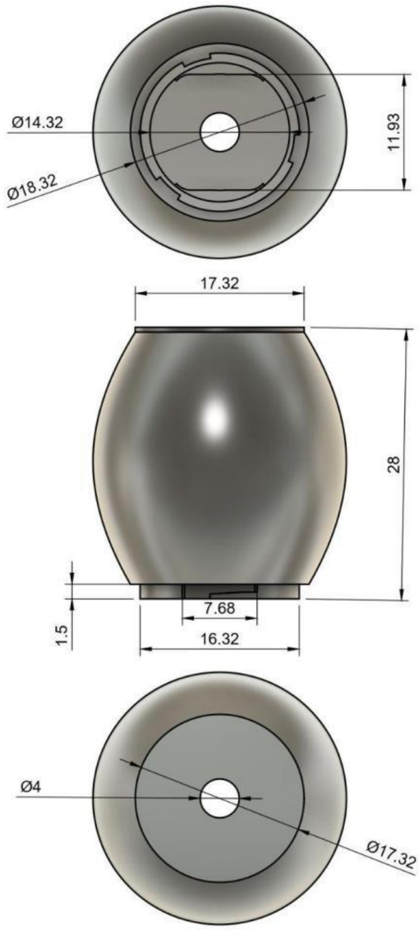

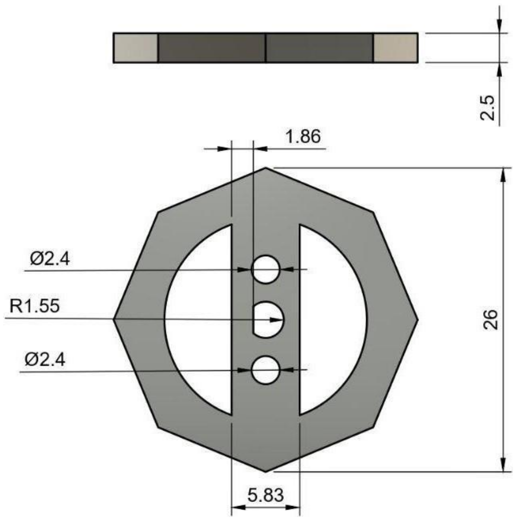

Fig 11. Spherical Enclosure

Fig 12. Octagonal Retainer Ring

The other components common to the variations discussed above are depicted in Figures 13, 14, 15, 16 and 17. Three locking mechanisms have been used to keep the assembly together. As discussed previously, the retainer ring locks itself on the shaft as well as constrains the axial motion of the enclosure since press fitting is involved. Secondly, there is the click and rotate locking mechanism, which secures the front and back lids to the front cover and enclosure, respectively. Small grooves have been designed on the front cover as depicted in Figure 13 that lock with the small extrusions designed on the front lid as represented in Figure 14. The third locking mechanism holds the front cover and the retainer ring together with the help of M2 bolt(s). This mechanism has been designed in two variations, which are depicted in figures 13 and 16, 17 respectively. The first design employs two M2 screws to secure the retainer ring's center shaft to the bottom surface of the front cover. Figures 8, 10, 12, and 13 show the screw location for the retainer ring and the front cover, respectively. Figures 16 and 17 show the second variation. A small cylindrical-shaped lock depicting a bearing is pressed against the surface of the front cover on the shaft. The lock has a thread for an M2 bolt that is screwed against the flat surface of the shaft to secure the lock. Figure 15 depicts the back lid, which has a hole in the center for wires used in tethered control. The back lid will also serve as a mount for the CCD camera.

Variation 1

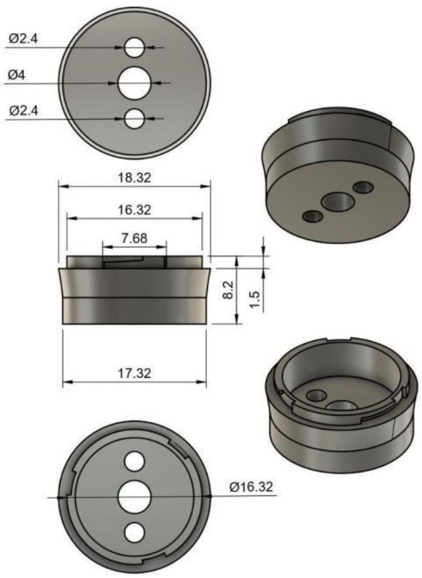

Fig 13. Front Cover Variation 1

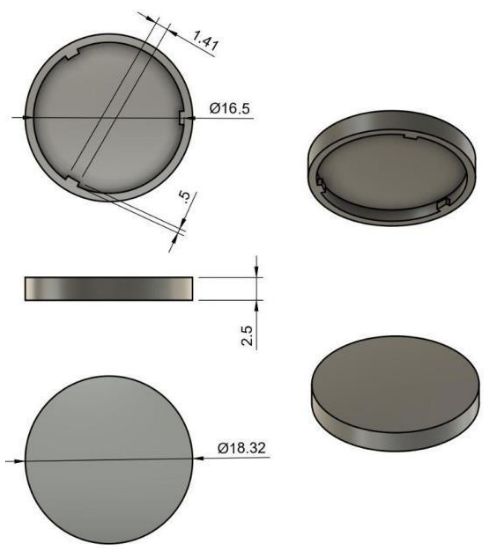

Fig 14. Front Lid

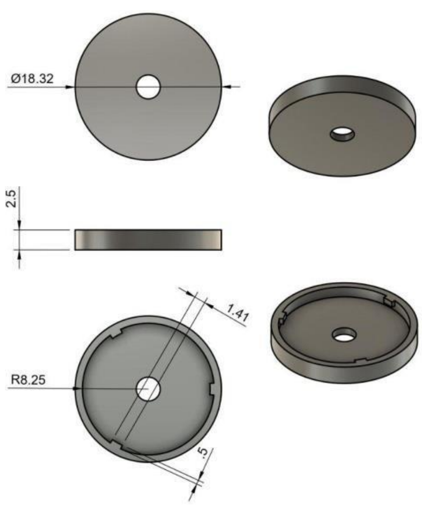

Fig 15. Back Lid

Variation 2

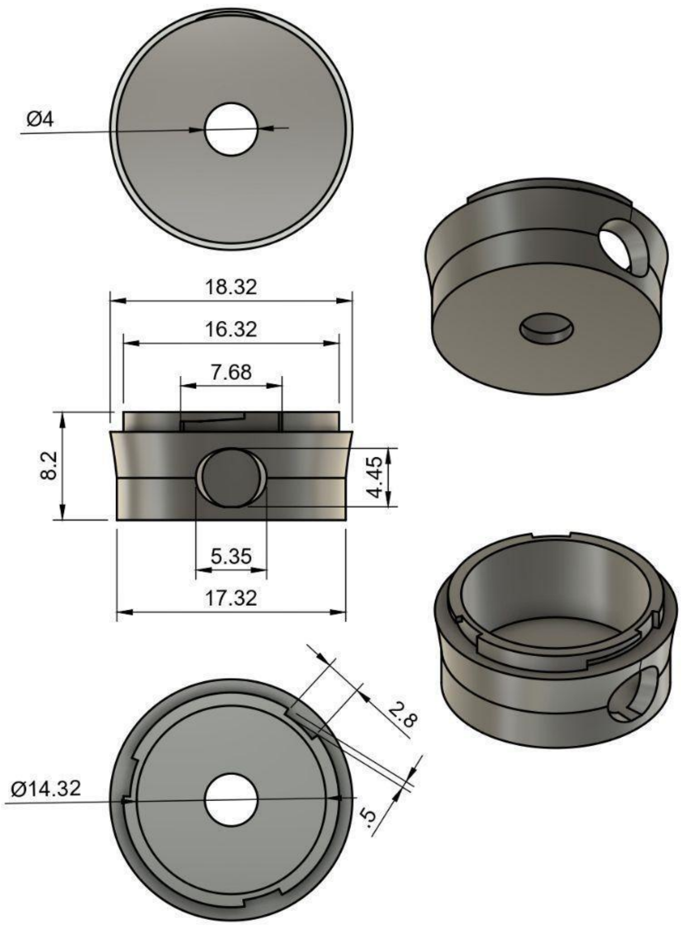

Fig 16. Front Cover Variation 2

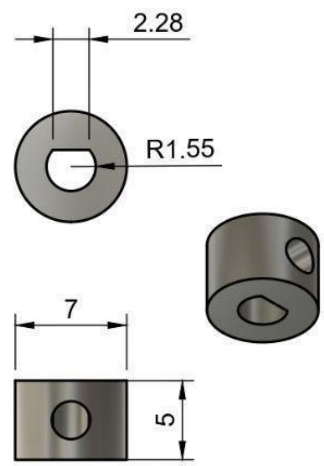

Fig 17. Lock

Fig 18 and 19 show the internal mechanism of the rolling prototype. The motor is mounted on an enclosure with inner extrusions to constraint radial motion. The retainer ring is heated and press fitted on the motor shaft against the enclosure to constraint the motor's axial motion. In the first design, the front cover is screwed with the retainer ring using M2 sized bolts to hold the assembly together. In the second design, a cylindrical lock is constrained to the flat side of the shaft by a M2 screw that holds the front cover against the retainer ring. The front and the back lid have small extrusions on the side which lock into place with the embossing provided on the front cover and the enclosure respectively.

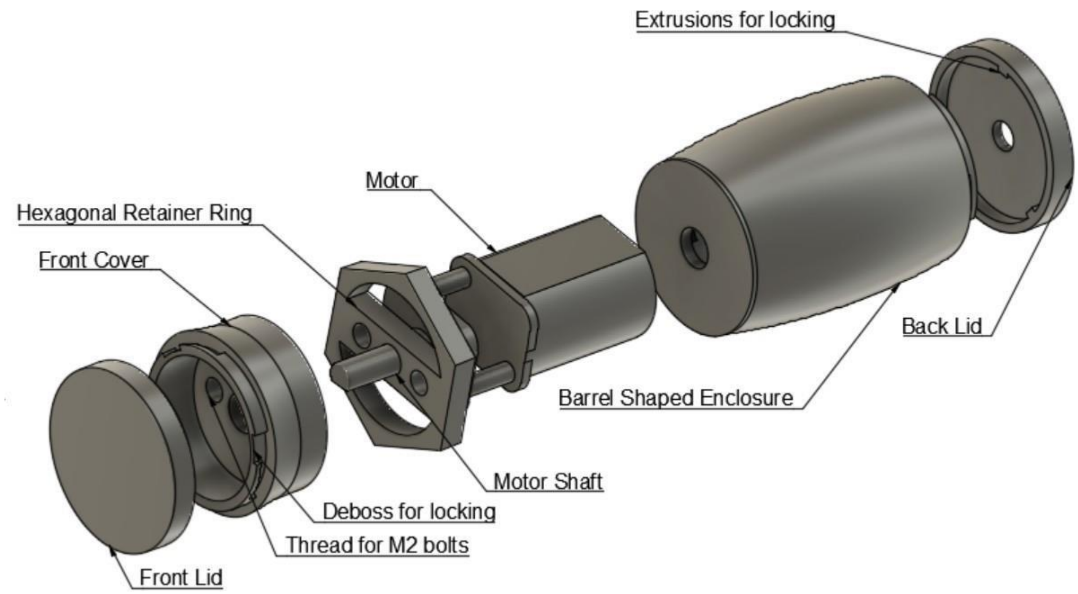

Fig 18. Disassembled View of Design one of the Rolling Segment of the Prototype

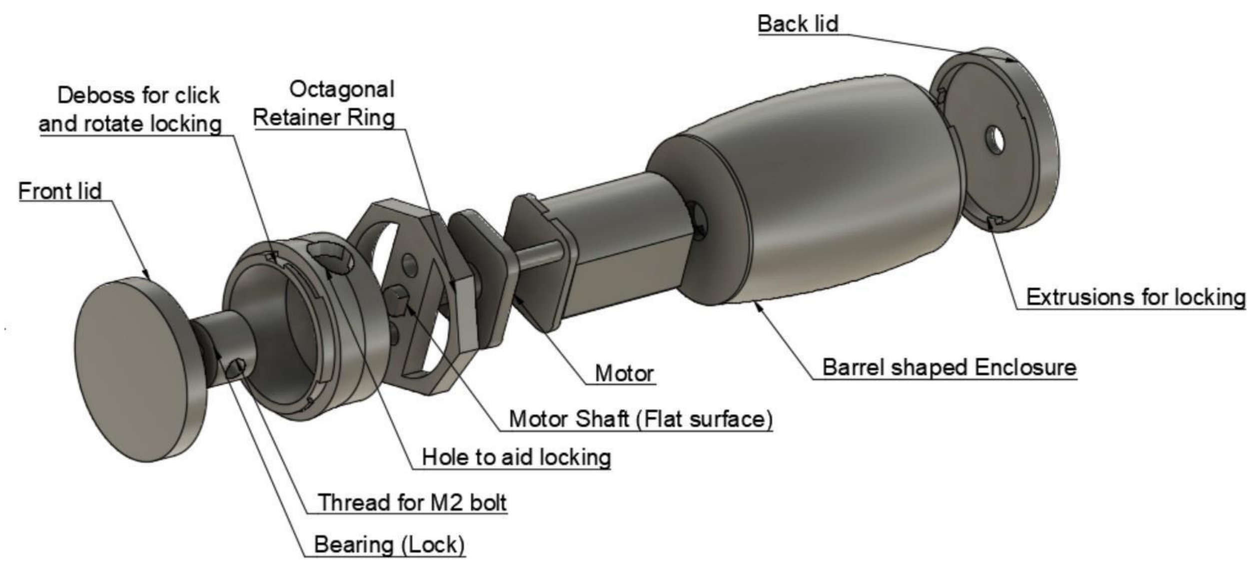

Fig 19. Disassembled View of Design two of the Rolling Segment of the Prototype

Project Synthesis

As discussed earlier, the “retainer ring” is the pivotal component that facilitates rolling motion of the entire assembly. Enough torque must be provided by the motor shaft to enable the rolling motion. The torque which has to be applied by the retainer ring on the ground is equal to summation of frictional torque and inertial torque. Fig. x shows various forces acting on the rolling segment when rolling freely using the ring mechanism.

We have,

W = weight of the rolling segment

$F_{friction}$ = Friction force between the rolling segment and the ground,

$T_{required}$ = Total torque required

$T_{friction}$ = Resisting Torque generated due to friction,

μ = coefficient of friction between the ground surface and the rolling segment outer surface, for aluminum and steel surface $\mu = 0.6$

We know that,

$F_{friction} = \mu \times W$

$T_{friction} = F_{friction} \times R$

Here,

R = outer radius of rolling segment = 0.02 m

$W = m \times g = 0.02 \times 10 = 0.2$ N

Here,

m = mass of rolling segment

g = acceleration due to gravity

For rotary movement of the rolling segment,

$T_{applied} = T_{friction} + T_{inertia}$

$T_{inertia} = I \times a$

Here,

I = Total moment of inertia of the rolling segment around axis of roll,

a = angular acceleration.

The inertial torque can be calculated by calculating summation of moment of inertia about axis of roll and multiplying it to required angular acceleration.

For the rolling motion desired or maximum angular speed that may be required is approximately

400°/s i.e. 6.9813^r/s. This desired speed should be reached within 1 seconds

∴ a = (5.236-0)/1 = 5.236 ^{r}/s^2

$T_{inertia}$ = 0.000002282 × 5.236 = 1.194 × 10^{-5} Nm.

$F_{friction}$ = 0.6 × 1.194 = 0.7169 N

$T_{friction}$ = 0.02 × 0.7169 = 0.01434 Nm.

Now, $T_{applied}$ = (0.01434) + (1.194 × 10^{-5}) = 0.01435194 Nm

Assuming safety margin of 1.5 for the motor torque,

T_{motor} = 1.5 × $T_{applied}$ = 1.5 × 0.01435194 = 0.02152791 Nm = 21.52791 mN.m

Table 2 Mass Properties for the components of the Rolling Segment

Sr No.	**Component**	**Mass**	**Radius of gyration**	**Moment of Inertia (I)**	**Moment of inertia**
		g	**mm**	**g.mm^2**	**kg.m^2**
1.	Front lid	1	19	361	3.61 x 10^{-7}
2.	Front Cover	2	15	450	4.5 x 10^{-7}
3.	Retainer Ring	1	10	100	1 x 10^{-7}
4.	Enclosure	4	5	200	2 x 10^{-7}
5.	Back lid	1	19	361	3.61 x 10^{-7}
6.	Motor	10	6	360	3.6 x 10^{-7}
7.	M2 screws (2)	2	15	450	4.5 x 10^{-7}
Total		20		2057	2.282 x 10^{-6}

CHAPTER 3: Kinematic and Static Modeling

Kinematic and static analysis of the prototype was done after developing the 3D CAD model in Fusion 360. Initially, the various components of the rolling assembly were designed only as per the size constraint and thus a kinematic and static study was required to test the practicality of the prototype.

Development of Kinematic Model

The kinematic model of the prototype Rolling Capsule was achieved using Solidworks software. Motion analysis was also attempted in the open source ADAMS® software but led to errors and thus could not be concluded. The modeling was done with the following technical considerations and preludes, viz.

1. Damping ratio was taken as $1x10^{-5}$
2. The weight of the motor assembly was assumed to be a lumped mass.
3. The speed of rotational motion that is to be generated for simulation should not exceed 500 rpm = 180000 degree/min = 3000 degree/sec = 52.35 rads/sec

Development of Static Model

Static modeling refers to Finite element analysis (FEA) of the critical components i.e., parts that may undergo failure during operation. FEA is a mathematical model of a physical system that includes a part or assembly, material properties, and boundary conditions. In numerous cases, simple hand calculations cannot mimic product behavior in the real world. FEA is a general technique for representing complicated behaviors by accurately capturing physical phenomena using partial differential equations. Here, the critical components (i.e., “retainer ring”) was analyzed for rheological parameters like stress, strain and deformation / deflection. This aspect of the simulations were carried out through the Finite Element Analysis (FEA) software, FEAST^{SMT}™.

One of the most crucial elements in conducting an accurate FEA simulation is meshing. A mesh is made up of elements that contain nodes (space coordinates that vary by element type) that represent the geometry's shape. The act of transforming irregular shapes into more recognisable volumes known as "elements" is known as meshing. The meshing results of the retainer ring are illustrated in Fig.

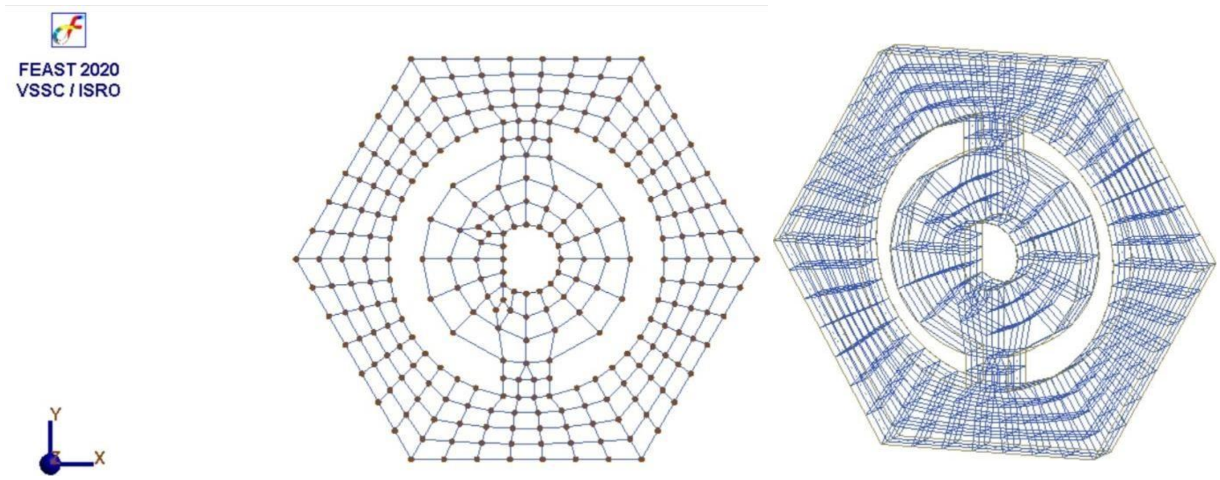

Fig 20. 2D and 3D meshing illustrations of the Retainer Ring. The nodes are represented in the first image as brown points.

The presence of imbalanced forces created during prototype operation, which could result in component failure, is the rationale for simulating a static analysis. In this situation, the retainer ring is restricted to the shaft and spinning at a high rpm. This causes an imbalanced centrifugal force, which can produce excessive deflection or strain during operation, leading to failure. Figure x depicts the constraints that must be applied to the component before the FEA solver may extract results.

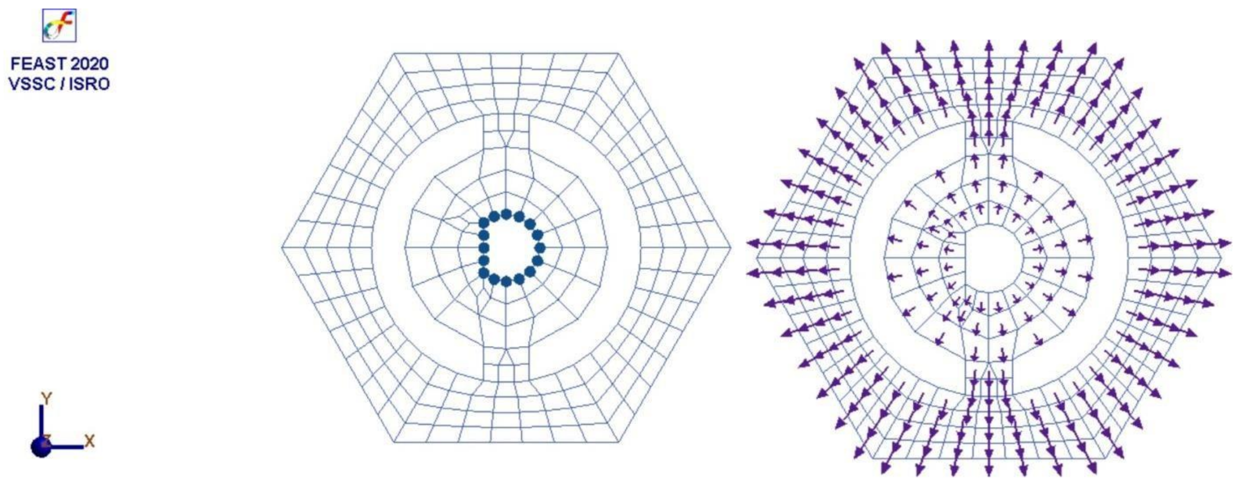

Fig 21. Constraints to be applied on the ring which may cause failure

Once the meshing is completed and all constraint parameters have been applied, the FEA solver is used to extract relevant results, as shown in Fig x, y, and z.

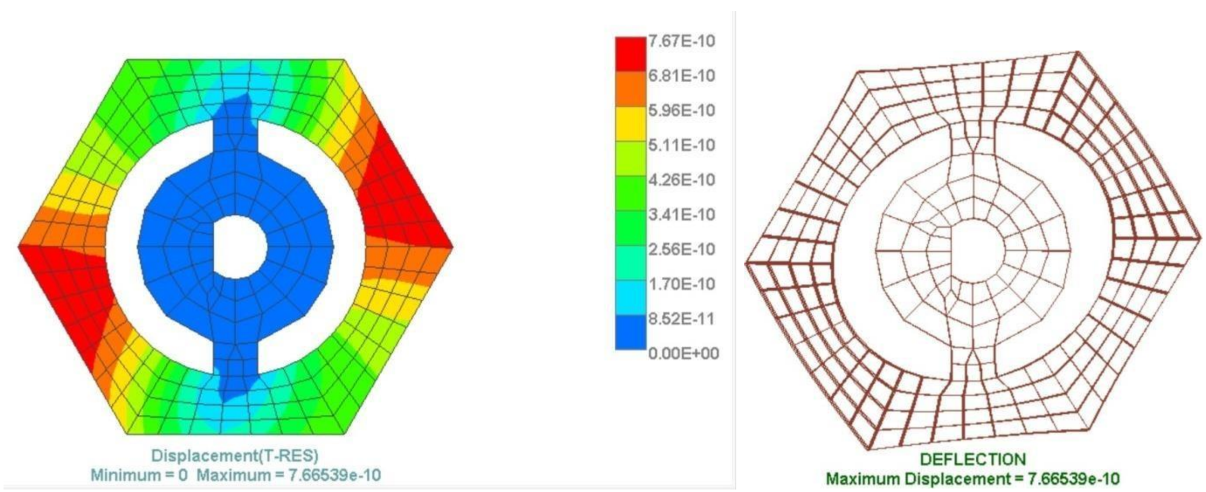

Fig 22. Displacement and Maximum Deflection Analysis Results

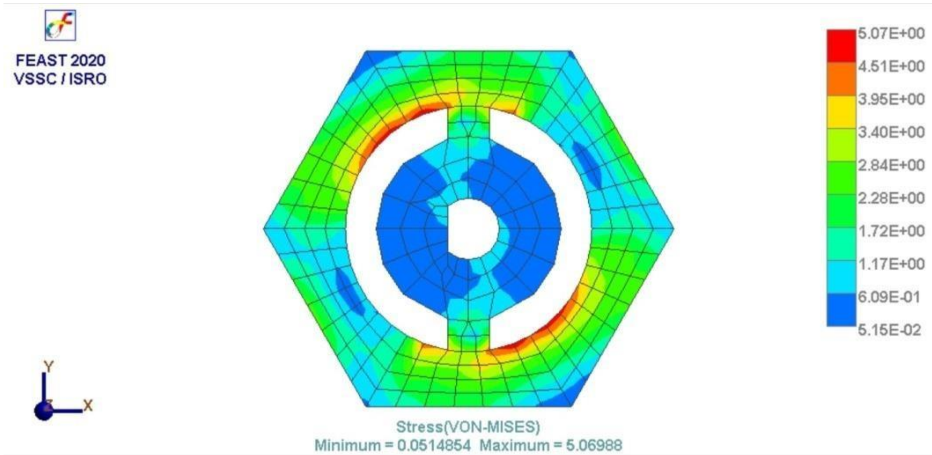

Fig 23. Stress Analysis of Retainer Ring in FEAST^{SMT} ™

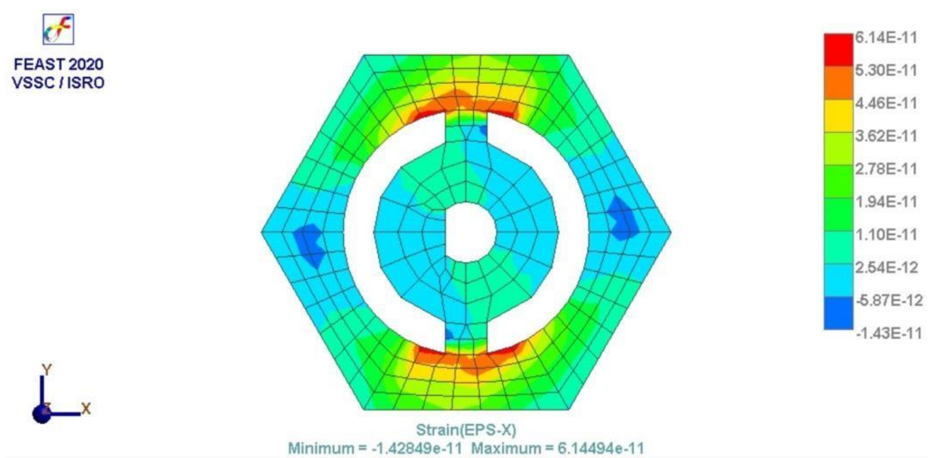

Fig 24. Strain Analysis of Retainer Ring in FEAST^{SMT} ™

From the results, it can be concluded that the deflection, stress and strain developed in the component during rotation will not result in fracture thus confirming the feasibility of the assumed speed.

CHAPTER 4: Manufacturing Details

The proposed designs were prototyped using metal 3D printed miniature components. Metal 3D Printing is an excellent method for producing miniature and detailed components. In terms of design reproducibility and economic feasibility, none of the existing manufacturing technologies are a match for Metal 3D Printing. Metal 3D Printing starts with creating a 3D CAD model, which is then "sliced" into several discrete layers. A heat source, usually a laser, partially melts the powdered metal base for each layer, which then binds with subsequent layers to formthree-dimensional objects. The Ultimaker Cura software was used to slice the CAD model created by Fusion 360. The 3D printing parameters were set in the same.

Creality Ender-3 3D printer as shown in Fig was used to print the miniature components described earlier. High standard V-profile and pulley for stable running, wear resistance, low noise, power supply protection etc are a few of its comprehensive features specifically designed to meet the prevalent industry needs of high productivity and serial production. PLA i.e. Polylactic Acid filaments were used for printing. PLA filament is a recyclable, natural thermoplastic polyester derived from renewable resources like corn starch or sugar cane. Under certain conditions, the filament is biodegradable and has a high heat capacity and mechanical strength.

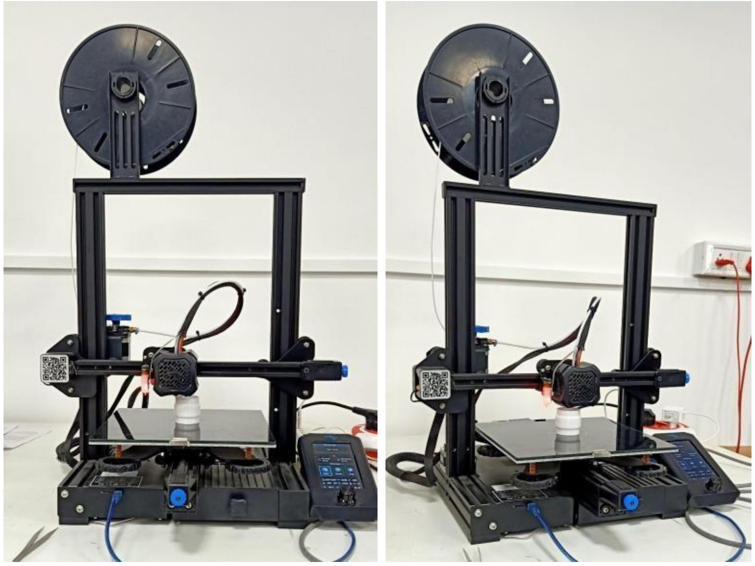

Fig 25. 3D Printing Device

The 3D printed components and final assembly are as illustrated below.

Fig 26. 3D printed Cylindrical, Barrel-shaped and Spherical Enclosures

Fig 27. 3D printed design variations of the two locking mechanisms

Fig 28. 3D printed final assemblies of possible enclosure variations

Troubleshooting:

The main challenge faced during the manufacturing process was 3D printer calibration. Since, miniature components were to be printed, even a 0.1 mm error resulted in inaccurate manufacture which in turn hindered final assembly of the prototype. Due to this, lots of components had to be re-designed and re-printed. Other reasons for manufacturing delays included minor warping or bending near the printer bed caused due to inaccurate bed-leveling, a messy first layer due to a non-sticky print, and inconsistent print due to filament becoming stuck inside the nozzle.

CHAPTER 5: Surface Defect Detection

As mentioned previously, the back lid of the rolling prototype will act as a mount for a CCD Camera which can then be used to capture images inside pipes which will in turn be used for offline inner surface inspection. We will be focusing on inner surface inspection of steel boiler tube pipes for the purpose of this study.

Overview

Steel is one of the most essential construction materials in today’s world due to its many unique advantages. However, the quality of steel can be adversely affected by common surface defects like pitting corrosion, pores, scabs, blisters, crazing, etc. The main reasons behind the formation of these defects can be attributed to the heavy machinery that meets a piece of steel before it is finally ready to be shipped. Thus, steel sheets should be inspected before the material is delivered

to assure optimal working conditions. Manual and automatic inspection are the two ways one can go about tackling this problem. However, the major drawback of manual inspection is the long hours it would take to produce accurate results. Hence, automating the inspection procedure would speed up the production of steel sheets. The objective of this study is to examine the Severstal Steel Defect dataset and to explore efficient methods to classify and label the faulty areas pixel by pixel.

Dataset

Deep learning methods rely on extensive and robust training data to enable them to generalize well. Since each new image brings a level of newness in terms of the features, the model's performance improves as the dataset of the manually annotated image examples grows. Constructing such a dataset is a time-intensive operation best left to the trained staff. Therefore, the dataset used in this is the open source Severstal Steel Defect Dataset [1]. This dataset consists of 6666 labeled images spread across four types of surface defects in steel plates. The ground truth segmentation masks are also provided in the form of run-length encoded pixels. Literature search reveals that one of the most widely used image segmentation models, namely, the original U-Net architecture, produces a dice coefficient less than 0.5 for this dataset, which is insufficient to justify the use of automation over manual inspection for defect detection. To overcome this discrepancy of needing automation but having poor automation results, the two-fold objective of this study is to first maximize the dice score while localizing the defect present in the image, and second, to maximize the multilabel classification probability estimates.

The Severstal Steel Defect dataset is used in this study, which consists of high-resolution images of steel sheets with four fault classes and areas. The dataset has a total of 6666 grayscale images, each with a resolution of 256 x 1600 pixels. Further, each image has a corresponding defect label and a run-length encoded ground truth segmentation map. Defects are categorized into four classes: type 1, type 2, type 3, and type 4. There are 897 photos with type 1 defects, 247 images with type 2 defects, 5150 images with type 3 defects, and 801 images with type 4 defects. The imbalance in the dataset is apparent from Fig. 29, which shows the class distribution. Out of 6666 images, 6239 images contain only one defect class, 425 images contain two defect classes, and only two images have three defect classes.

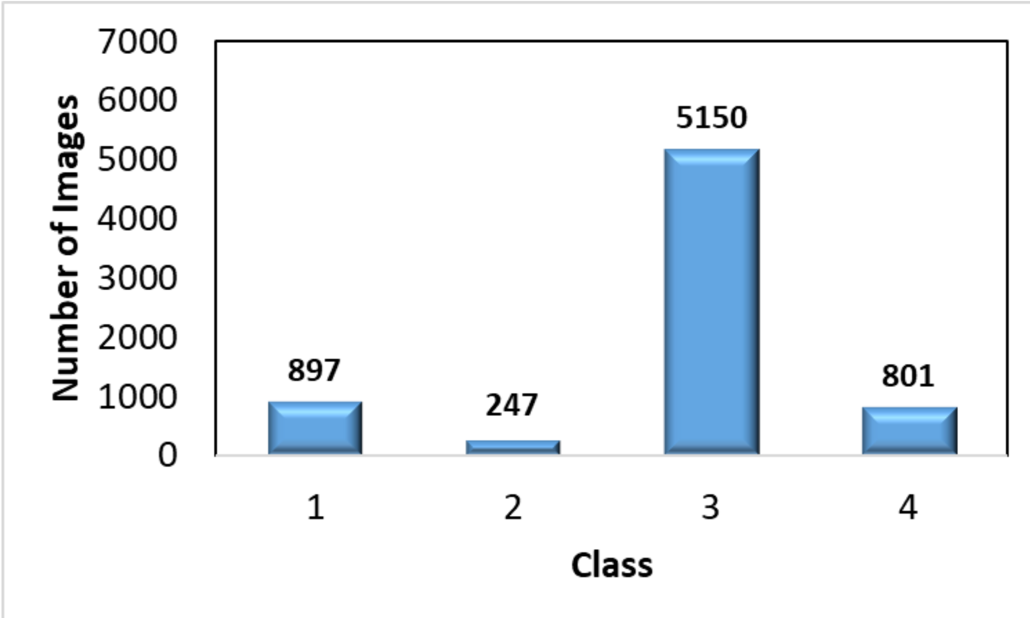

Fig 29. Bar graph showing imbalance between the number of images in each defect class.

Two samples for each defect type from the dataset are shown in Fig 30. It is observed that many tiny size regions are present in type 1 defect type 1 photos, whereas multiple medium-size regions are present in type 4 defects. Multiple medium-sized regions are also visible type 3 defects. While the images of defect type 2 and type 3 share some regional characteristics, they are not identical.

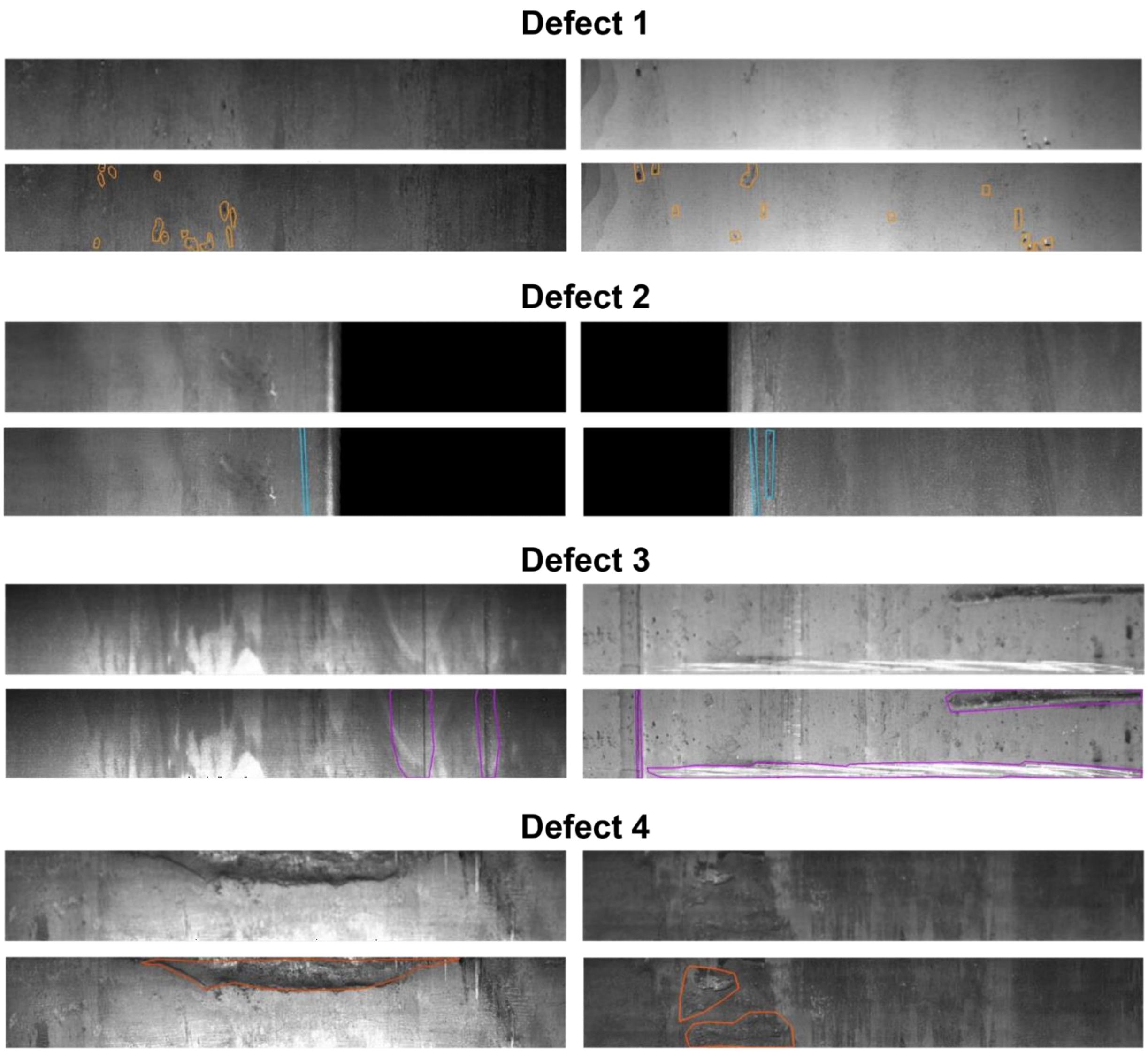

Fig 30. Representative images of surface defects in steel plates provided in the Severstal Steel Defect Detection Dataset [1]. Top row in each defect shows raw images. The defects detected after processing are shown marked in bottom images.

Methodology

Multilabel classification and semantic segmentation are explored separately for defect detection in steel plates (see Fig. 31). Semantic segmentation can generate pixel-wise masks of defects whilst classifying it under a class label. Therefore, a baseline fully connected network is trained as baseline and the pertinent modifications are made to the well-known U-Net architecture to optimize the dice scores further. To validate the classification results of the segmentation models, both single and multi-output CNN-based architectures are explored. Even though the classification does not indicate exact location of the defect, it can aid in manual localization because of its high accuracy.

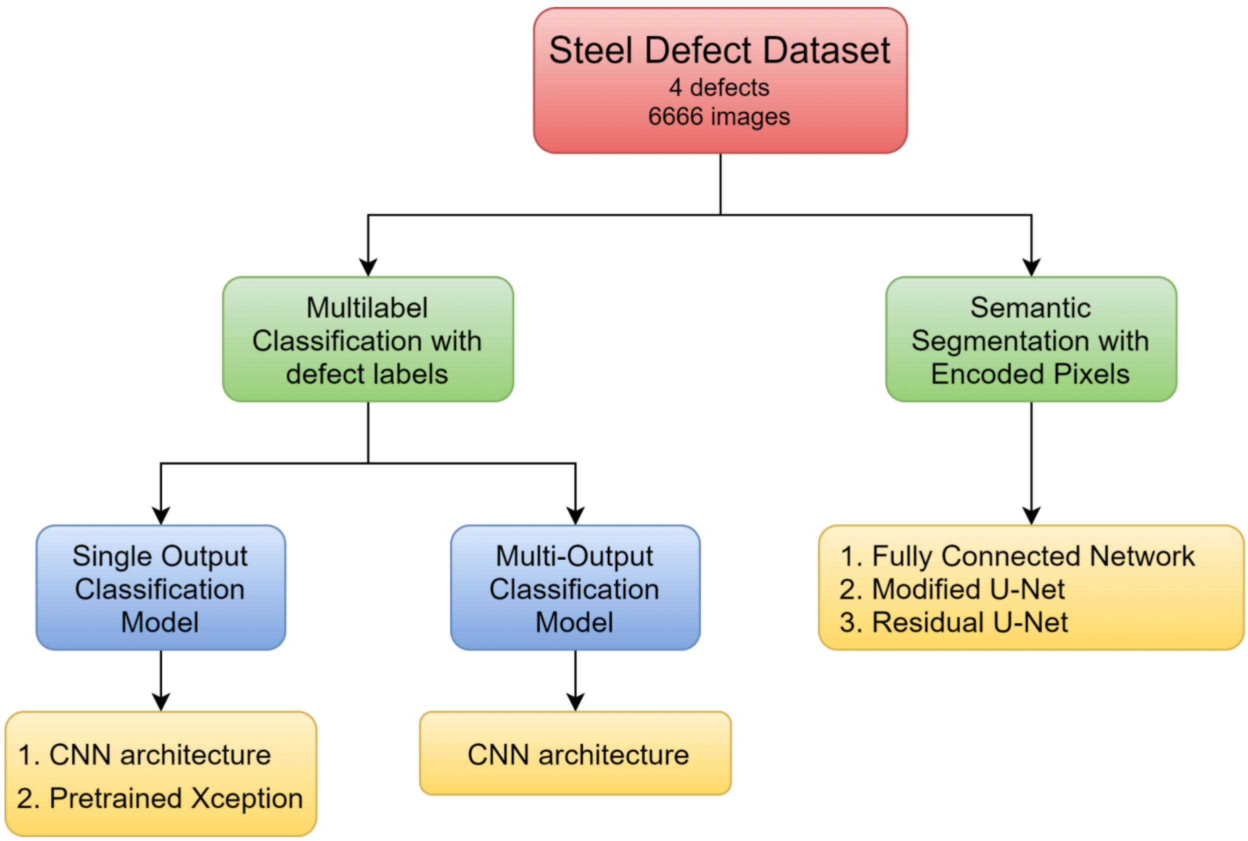

Fig 31. Flowchart showing the methodology adapted for detecting surface defects in steel plates using deep learning-based multilabel image segmentation and classification techniques.

Results and Inference

The accuracy and loss curves are plotted across epochs for the trained classification models, which allow the training progress of the networks to be observed. These plots also help in understanding how well a given model generalizes. If the gap between the validation line and the training line increases with time, with the validation scores lagging, it can be inferred that the model is overfitting the training data. This means that the model is getting good at learning the intricacies of the training data but at the cost of losing its generalizability over the new data. Similarly, if the training scores start lagging, the model is said to be under-fitted. From Fig. 32, it is apparent that all the plots exhibit a good generalization potential with a steady increase in the prediction accuracy.

Multilabel Classification

As discussed previously, two single output classifiers are trained for 50 epochs with an early stopping callback. Their validation accuracy is monitored with a patience of 10 for the callback. Fig. 32 shows the binary cross-entropy loss and the accuracy plotted as a function of epochs of the trained models.

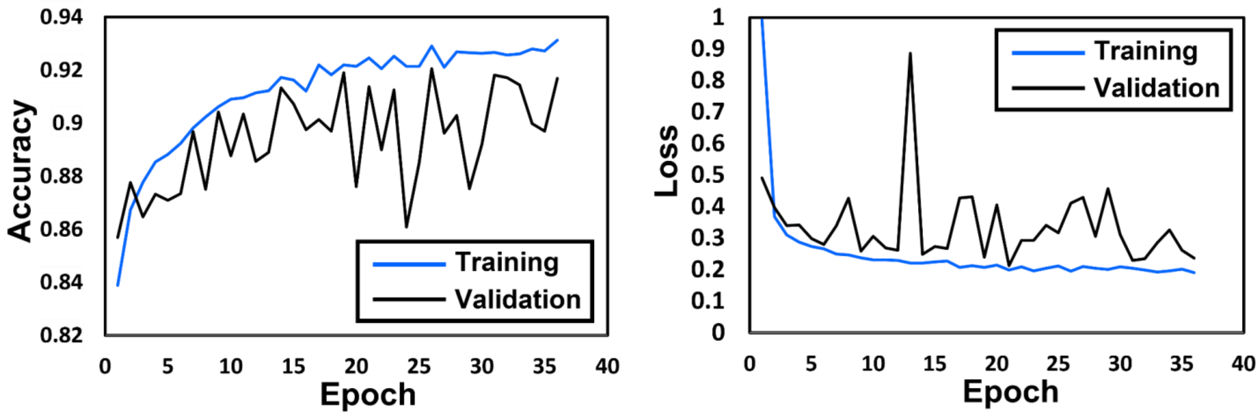

Fig. 32. The accuracy (left) and loss (right) curves for a single output CNN Classifier

Single Output Classifiers

It can be observed from Fig 32 that the CNN classifier is trained for 36 epochs and indicates that a maximum accuracy of 92.045% was achieved at the 26th epoch. The batch size used for training is 32. The gradually decreasing trend of the loss curve and corresponding increasing trend of the accuracy curve implies that the model is learning over each epoch.

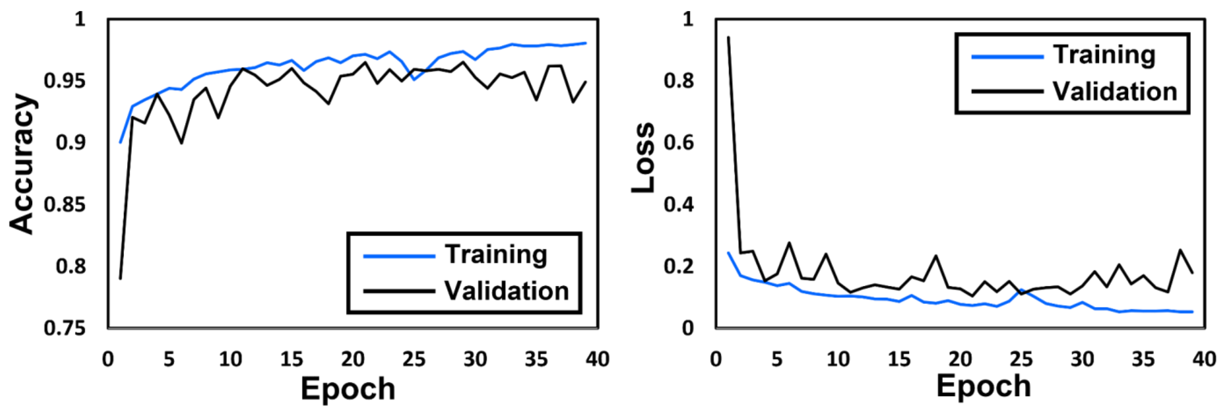

Fig. 33. Accuracy (left) and loss (right) curves of pre-trained Xception Classifier

Fig 33 provides an estimate of the training progress of the Xception classifier. It is evident that the Xception classifier is trained for 39 epochs and that the maximum accuracy of 96.513% is achieved at the 29th epoch. The corresponding loss value is 0.0672. Note that the Xception classifier surpasses the accuracy obtained using the CNN classifier at the 3rd epoch itself, thus showcasing the superiority of transfer learning approach. Furthermore, the validation curves show fewer fluctuations, which implies a more stable learning curve compared to the CNN classifier.

Multi-Output CNN Classifier

Table 3. Accuracy scores and loss of multi-output model for each defect

	Defect 1	**Defect 2**	**Defect 3**	**Defect 4**
Accuracy	0.9318	0.9804	0.8781	0.9535
Loss	0.2119	0.0717	0.3335	0.1474

Table 3 summarizes the evaluation metric of the multi-output CNN classifier. It is observed that in the overall accuracy of 92.045% for the single output classifier, the classification of defect 2 contributes the most. Despite the lowest number of images in defect 2 and the highest number of images in defect 3, their accuracies are the highest and lowest respectively. The way this observation can be understood is to use the re-weighting method from the scikit-learn library to estimate the individual class weights for the unbalanced dataset. In short, the lower the data in a certain class, the higher weight it gets. This influences the loss function by assigning relatively higher costs to the examples from the minority classes. However, this method did not show any noticeable increase in the scores. Therefore, the high validation accuracy of the minority class can be attributed to the less variation in data of class 2 defects. On the other hand, even though defect 3 has a larger database, the inter-class variability results in a lower score.

Image Segmentation

Figures 34, 35 and 36 illustrate the plots of dice coefficient and the validation loss as a function of epochs for the three trained segmentation models i.e., FCN model, Hyper-tuned Modified U-Net and residual U-Net, respectively.

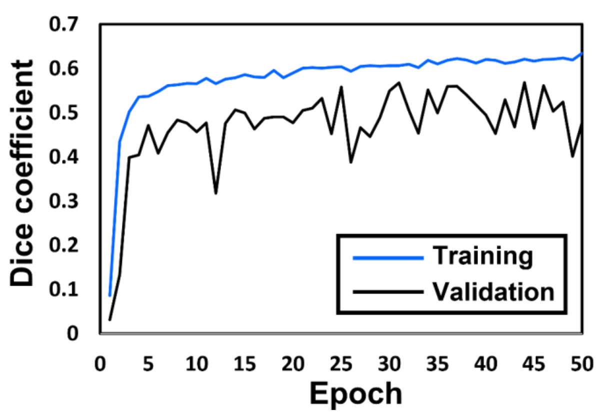

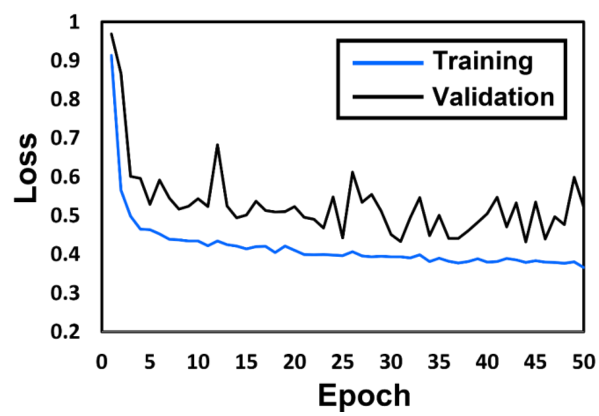

Fig. 34. Dice and Loss coefficient plots of the FCN Model

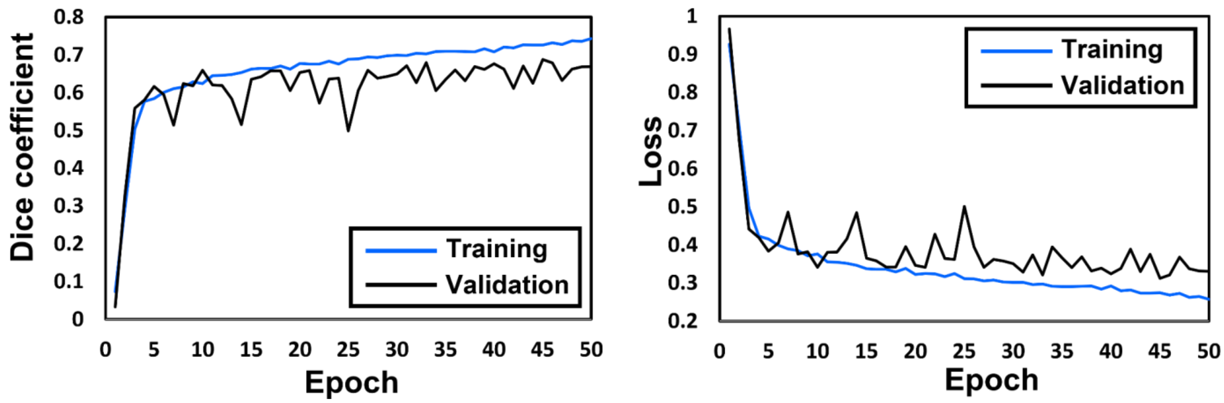

Fig. 35. Dice and Loss coefficient plots of the Hyper-tuned Modified U-Net Model

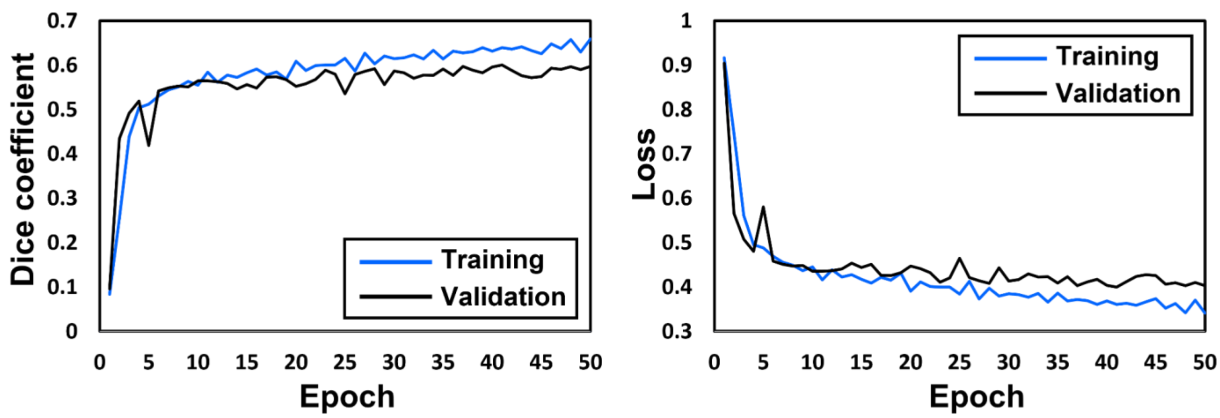

Fig. 36. Dice and Loss coefficient plots of Residual U-Net Model

All the models were trained for 50 epochs with a batch size of 32. The baseline model i.e., the fully connected network gives a dice score of 0.5672. The loss value of the validation sets is like the training set for hyper-tuned modified U-Net as well as the residual U-Net, indicating that the models will generalize well with the other sets. Hyper-tuned modified U-Net shows the best results with a dice coefficient of 0.69. The slow but a steady increase in the dice coefficient of residual U-Net indicates that training for more time may give better results. It is also important to note that the additional batch Normalization and the dropout layers for hyper-tuned modified U-Net and the Residual U-net result in a much stable learning curve with minimal fluctuations in validation.

Table 4. Metrics of segmentation models

Sr No.	METRICS	PROPOSED MODELS		
		FCN	Hyper-tuned modified U-NET	Residual U-NET
1	Dice Coefficient	0.5672	0.6888	0.60027
2	Precision	0.6065	0.7191	0.6941
3	Recall	0.5499	0.6682	0.5388
4	Mean IoU	0.4027	0.5277	0.4338

Table 4. summarizes the evaluation metrics used for comparing the segmentation models. Other than the dice coefficient, three other metrics, namely precision, recall, and mean IoU scores are also monitored. Precision scores help in understanding as to how many relevant predictions the model can make. For example, whenever the hyper-tuned modified U-Net model predicts a pixel as being defective, it is correct 71.91% of the time. Recall scores provide an estimate of the model correctly identifying the pixels with defects. Mean IoU scores specify the amount of overlap between the predicted and the ground truth. Overall, the hyper-tuned modified U-Net model is superior in all aspects.

Conclusion

The surface imperfections of steel are the subject of this chapter's investigation. The dataset explored in the work is obtained from Severstal. The exploratory data analysis (EDA) of the dataset reveals that a single image may contain one or more defects, thus presenting a problem statement of multilabel classification and segmentation. EDA also demonstrates that there is a significant class imbalance within the dataset, which is addressed using data augmentation, class-wise re- weighing and adaptive learning rate methods. A multi-output model is also trained to get an estimate of how the data imbalance is affecting the overall accuracy of a single output network. Since pixel-wise defect masks are also provided in the dataset, three multilabel segmentation models are trained with an aim of maximizing the dice coefficient. A fully connected network that achieves a dice score of 0.5672 is treated as the baseline model. The other two segmentation models are inspired by the well-reported U-Net architecture. The original encoder-decoder network with skip connections is hyper-tuned and modified by adding new learning layers and activation functions as part of the first modification. In the second method, the U-Net is strengthened with the help of residual learning. Amongst the segmentation models, the hyper-tuned modified U-Net design achieves a dice score of 0.69, whereas the Residual U-Net shows promising results as is observed from its smooth training curve. With a final dice score of 0.69 on the best model (which is an increase of 0.2 from the original U-Net structure), the objective of this study is successfully fulfilled.

CHAPTER 6: Future Scope

The present study summarizes the research, development, and testing of a miniature tethered 3D printed rolling prototype capable of traversing horizontally in a pipeline with a diameter as small as 50 mm for its internal inspection. Since the main challenge addressed in this study was miniaturization, a few other factors took a back seat. The primary constraint of the current prototype is its tethered control system which limits the range since long wires inside long twisted pipelines may result in entanglement. Thus, wireless control systems that maintain the level of miniaturization are an intriguing direction for future work to make the robot function robustly. Secondly, the current prototype is only capable of traversing horizontally which limits its inspection capabilities. A separate or connected crawling segment capable of moving vertically can be added to the current rolling prototype to increase its range of motion.

Due to time constraints, experimentation with a functioning camera segment design could not be conducted. Procurement of a miniature CCD camera and designing of a mount for the same can be the next required steps. Finally, the current offline deep learning image-based inspection algorithm relies on a small open-source dataset. Efforts can be made to obtain a more diverse and relevant dataset that corresponds to the surfaces on which the prototype is tested.

References

[1] Hajjaj, S. S. H., & Khalid, I. B. (2018). Design and development of an inspection robot for oil and gas applications.

[2] Wahed, M. A. A., & Arshad, M. R. (2017, October). Wall-press type pipe inspection robot. In *2017 IEEE 2nd International Conference on Automatic Control and Intelligent Systems (I2CACIS)* (pp. 185-190). IEEE.

[3] Ogai, H., & Bhattacharya, B. (2018). Pipe inspection robots for gas and oil pipelines. In *Pipe Inspection Robots for Structural Health and Condition Monitoring* (pp. 13-43). Springer, New Delhi.

[4] Aitken, J. M., Evans, M. H., Worley, R., Edwards, S., Zhang, R., Dodd, T., ... & Anderson, S. R. (2021). Simultaneous localization and mapping for inspection robots in water and sewer pipe networks: A review. IEEE Access.

[5] Ray, D. N. (2021, June). Slim and Expandable Header Inspection Robot for Remote Visual Inspection of Boiler Headers in Thermal Power Plants. In *Advances in Robotics-5th International Conference of The Robotics Society* (pp. 1-8).

[6] Tătar, O., Mandru, D., & Ardelean, I. (2007). Development of mobile minirobots for in pipe inspection tasks. *Mechanika*, *68*(6).

[7] Kaiwart, A., Dubey, N. D., Naseer, F., Verma, A., & Pradhan, S. (2022). Design of Adaptive Wheel Driven Pipeline Inspection Robot. In *Advances in Mechanical Engineering and Technology* (pp. 583-595). Springer, Singapore.

[8] Bulnes, F. G., Usamentiaga, R., García, D. F., & Molleda, J. (2012). Vision-based sensor for early detection of periodical defects in web materials. Sensors, 12(8), 10788-10809.

[9] Yun, J. P., Choi, S., & Kim, S. W. (2009). Vision-based defect detection of scale-covered steel billet surfaces. Optical Engineering, 48(3), 037205.

[10] Martín, D., Guinea, D. M., García-Alegre, M. C., Villanueva, E., & Guinea, D. (2010). Multi-modal defect detection of residual oxide scale on a cold stainless-steel strip. Machine Vision and Applications, 21(5), 653-666.

[11] Severstal: Steel defect detection: [https://www.kaggle.com/c/severstal-steel-defect-detection/data]